



# Correlated states in twisted double bilayer graphene

Cheng Shen<sup>1,2</sup>, Yanbang Chu<sup>1,2</sup>, QuanSheng Wu<sup>3,4</sup>, Na Li<sup>1,2</sup>, Shuopei Wang<sup>1,5</sup>, Yanchong Zhao<sup>1,2</sup>, Jian Tang<sup>1,2</sup>, Jieying Liu<sup>1,2</sup>, Jinpeng Tian<sup>1,2</sup>, Kenji Watanabe<sup>6</sup>, Takashi Taniguchi<sup>6</sup>, Rong Yang<sup>1,5,7</sup>, Zi Yang Meng<sup>1,5,8</sup>, Dongxia Shi<sup>1,2,7</sup>, Oleg V. Yazyev<sup>3,4</sup> and Guangyu Zhang<sup>1,2,5,7</sup>✉

**Electron-electron interactions play an important role in graphene and related systems and can induce exotic quantum states, especially in a stacked bilayer with a small twist angle<sup>1–7</sup>. For bilayer graphene where the two layers are twisted by the ‘magic angle’, flat band and strong many-body effects lead to correlated insulating states and superconductivity<sup>4–7</sup>. In contrast to monolayer graphene, the band structure of untwisted bilayer graphene can be further tuned by a displacement field<sup>8–10</sup>, providing an extra degree of freedom to control the flat band that should appear when two bilayers are stacked on top of each other. Here, we report the discovery and characterization of displacement field-tunable electronic phases in twisted double bilayer graphene. We observe insulating states at a half-filled conduction band in an intermediate range of displacement fields. Furthermore, the resistance gap in the correlated insulator increases with respect to the in-plane magnetic fields and we find that the  $g$  factor, according to the spin Zeeman effect, is  $\sim 2$ , indicating spin polarization at half-filling. These results establish twisted double bilayer graphene as an easily tunable platform for exploring quantum many-body states.**

Twisted bilayer graphene (TBG) with a small twist angle,  $\theta$ , exhibits a significantly reconstructed band structure<sup>1–3</sup>. In the vicinity of the magic angle at  $\theta \approx 1.1^\circ$ , strong interlayer hybridization leads to the formation of a flat band with low energy and narrow bandwidth, and greatly enhances the electronic interaction effect<sup>1,4–7</sup> compared to graphene and bilayer graphene without twisting<sup>8</sup>. In TBG, correlated insulating states and unconventional superconductivity have been observed for a variety of partially filled bands<sup>4–7</sup>, and phenomena such as ferromagnetism and the quantum anomalous Hall effect<sup>7,11–13</sup>, topological phases<sup>14,15</sup> and features resembling those of a high-temperature superconductor<sup>5,16</sup> have been explored extensively<sup>17–19</sup>. However, to observe these interesting correlation-induced phenomena in TBG, one has to accurately control  $\theta$ , which puts strict constraints on device fabrication. Accordingly, achieving easier access to the flat band by means of alternative approaches is of great importance. Recently, a correlated insulator and superconductivity have been observed in TBG with  $\theta > 1.2^\circ$  on exerting high external pressure<sup>6</sup>. By applying vertical electrical fields, similar behaviour can also be achieved in ABC-stacked trilayer graphene on hexagonal boron nitride (hBN)<sup>20–22</sup>. Unfortunately, applying a

displacement field to modulate the bandwidth of the flat band in TBG has little effect due to its strong interlayer hybridization<sup>1,3,6</sup>.

Twisted double bilayer graphene (TDBG), on the other hand, is also likely to possess a flat band and display correlated phenomena. It is known that monolayer graphene possesses linearly dispersive energy bands showing no dependence on a displacement field. In contrast, Bernal (AB)-stacked bilayer graphene shows parabolic band dispersion, and gap opening at the charge neutral point (CNP) could be induced under displacement fields<sup>8–10</sup>. The gap reaches its minimum close to (although not exactly at) the K point, displaying a sombrero-shaped band structure dispersion<sup>8,10</sup>, which facilitates the formation and tunability of the flat band in TDBG.

In this work, we report the successful control of the electronic phases in TDBG by vertical displacement fields. In a specific range of displacement fields, we observe correlated insulating states corresponding to the half-filled conduction band. Moreover, under parallel magnetic fields, we find that the correlated gap for the half-filled band increases, suggesting spin-polarized ordering.

Figure 1a presents a schematic of the structure of our dual-gate devices (for details of device fabrication, see Methods). Under appropriate displacement fields, the reconstructed band structure of AB-stacked bilayer graphene shows a more pronounced flatness at the top of the valence band and bottom of the conduction band, thus facilitating formation of the flat band in TDBG (Fig. 1b). Figure 1c shows a typical band structure resulting from tight-binding calculations based on ab initio parameters. We can clearly see the well-isolated flat conduction band under an intermediate displacement field.

We tested many dual-gated devices with  $\theta$  varying from  $0.98^\circ$  to  $1.33^\circ$  to reveal transport behaviour in TDBG (Extended Data Fig. 1). All the devices show single-particle gaps at a superlattice density of  $n = \pm n_s$  on both electron and hole branches (Fig. 1d and Extended Data Fig. 1) as well as displacement field-induced gaps at the CNP due to the Bernal-stacked lattice structure of the original bilayer graphene. Note that higher-order superlattice gaps at  $n = \pm 3n_s$  can be observed in devices with a smaller  $\theta$  of  $\sim 1.0^\circ$ . The twist angle can be extracted from its relation with superlattice carrier density  $n_s$  (for more details see Methods). The dual-gate structure makes it easier to independently tune the carrier density as well as the displacement field across the TDBG. The displacement field and carrier density are given by  $D = \frac{1}{2}(D_b + D_t)$  and  $n = (D_b - D_t)/e$ , where

<sup>1</sup>Beijing National Laboratory for Condensed Matter Physics and Institute of Physics, Chinese Academy of Sciences, Beijing, China. <sup>2</sup>School of Physical Sciences, University of Chinese Academy of Sciences, Beijing, China. <sup>3</sup>Institute of Physics, Ecole Polytechnique Fédérale de Lausanne (EPFL), Lausanne, Switzerland. <sup>4</sup>National Centre for Computational Design and Discovery of Novel Materials MARVEL, Ecole Polytechnique Fédérale de Lausanne (EPFL), Lausanne, Switzerland. <sup>5</sup>Songshan Lake Materials Laboratory, Dongguan, Guangdong, China. <sup>6</sup>National Institute for Materials Science, 1-1 Namiki, Tsukuba, Japan. <sup>7</sup>Beijing Key Laboratory for Nanomaterials and Nanodevices, Beijing, China. <sup>8</sup>HKU-UCAS Joint Institute of Theoretical and Computational Physics, Department of Physics, The University of Hong Kong, Hong Kong, China. ✉e-mail: [gyzhang@iphy.ac.cn](mailto:gyzhang@iphy.ac.cn)

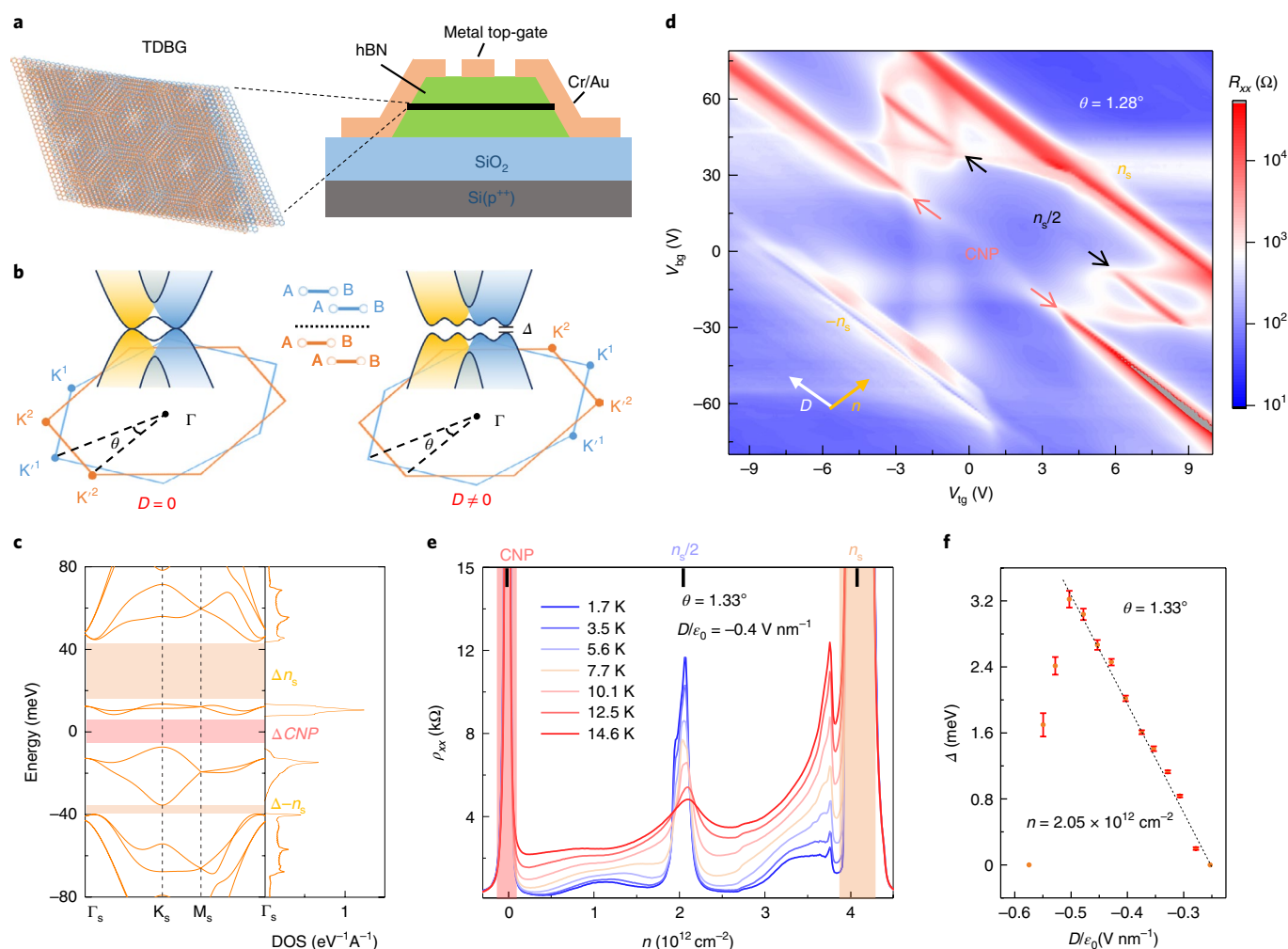


**Fig. 1 | Correlated insulating states at half-filling tuned by displacement fields.** **a**, Schematic of a moiré unit cell in TDBG (left) and the device structure (right). **b**, Illustration of the electrical tuning mechanism. Two parabolic dispersive bands from original Bernal-stacked bilayer graphene layers are displaced by twist angle  $\theta$  (left, without displacement field  $D$ ). Sombrero-shaped bands in each bilayer graphene are induced by non-zero  $D$  (right). The middle sketch presents the cross-sectional configuration of AB-AB-stacked TDBG. **c**, Calculated band structure of TDBG with  $\theta = 1.3^\circ$  in a vertical electrical field  $|E| = 50 \text{ mV nm}^{-1}$ , which corresponds to  $|D|/\epsilon_0 \approx 0.2 \text{ V nm}^{-1}$  by adopting a dielectric constant of hBN without considering the screening effect in TDBG. The horizontal colour bars indicate various single-particle bandgaps. The right panel plots the density of state (DOS) at different energies. Here,  $A$  is the area of the moiré unit cell. **d**, Colour plot of four-probe resistance versus metal top-gate and Si back-gate voltages in the  $1.28^\circ$  device at  $T = 4 \text{ K}$ . **e**, Temperature-dependent four-probe resistivity  $\rho_{xx}$  versus carrier density  $n$  in the  $1.33^\circ$  device. Temperature  $T$  varies from  $1.7 \text{ K}$  (dark blue curve) to  $14.6 \text{ K}$  (dark red curve). **f**, Thermal activation gap at half-filling in the  $1.33^\circ$  device as a function of displacement field  $D$ . The gap is fitted with Arrhenius formula  $R \approx \exp(\Delta/2kT)$ . The dashed line denotes nearly linear enhancement of the half-filling correlated gap with respect to  $D$ . Error bars are estimated from the uncertainty in the range of the simply activated regime.

$D_b = +\epsilon_0 \epsilon_{rb} (V_b - V_b^0)/d_b$  and  $D_t = -\epsilon_0 \epsilon_{rt} (V_t - V_t^0)/d_t$ , and  $\epsilon_{rb}$  and  $\epsilon_{rt}$  are the relative dielectric constants for the bottom dielectric layer with thickness  $d_b$  and top dielectric layer with thickness  $d_t$ , respectively. In our devices, the dielectric layers are composed of  $\text{SiO}_2$  and hBN (Fig. 1a), both of which share the same relative dielectric constant  $\epsilon_r \approx 3.9$ .  $\epsilon_0$  is the permittivity of vacuum and  $V_b^0$  and  $V_t^0$  are the offset gate voltages required to reach charge neutrality.

With an intermediate  $D$ , we can see an obvious resistive state at  $n = n_g/2$  where a moiré unit cell is filled with two electrons (Fig. 1d), so that the single-particle conduction band located between charge neutrality and the conduction superlattice band is half-filled. The asymmetry between the flat conduction and valence bands presumably arises from an intrinsic particle-hole asymmetry in the original Bernal-stacked bilayer graphene<sup>23</sup>. Figure 1e shows definite insulating behaviour of the half-filling state below  $T \approx 15 \text{ K}$  at  $D/\epsilon_0 = -0.4 \text{ V nm}^{-1}$  (marked in Extended Data Fig. 1) in

a  $1.33^\circ$  device. This characteristic temperature is higher than most reported results for TBG<sup>4–7</sup>. By fitting with the Arrhenius formula  $R \approx \exp(\Delta/2kT)$ , the gap of the half-filling state in the  $1.33^\circ$  device is estimated in Fig. 1f; it shows strong dependence on the displacement field and a maximum value of  $\sim 3.2 \text{ meV}$ . Note that the fitted gap at half-filling also varies with twist angle. According to our results, the regime of  $1.2\text{--}1.3^\circ$  produces observable insulating behaviour above liquid helium temperature.

The induced gap at half-filling is widely observed within the regime of  $|D|/\epsilon_0 = 0.2$  to  $\sim 0.6 \text{ V nm}^{-1}$  (Figs. 1e and 2a) and features non-monotonic change with respect to the displacement field. As  $D$  increases, the single-particle gap at CNP ( $\Delta_{\text{CNP}}$ ) increases monotonously, while at  $n = \pm n_g$  ( $\Delta_{\pm n_g}$ ) it decreases because of the electrostatic potential difference (Extended Data Figs. 2 and 3). The isolated flat band, flanked by these single-particle gaps at CNP and  $\pm n_g$ , is closely related to the gap size. Our data confirm that the correlated

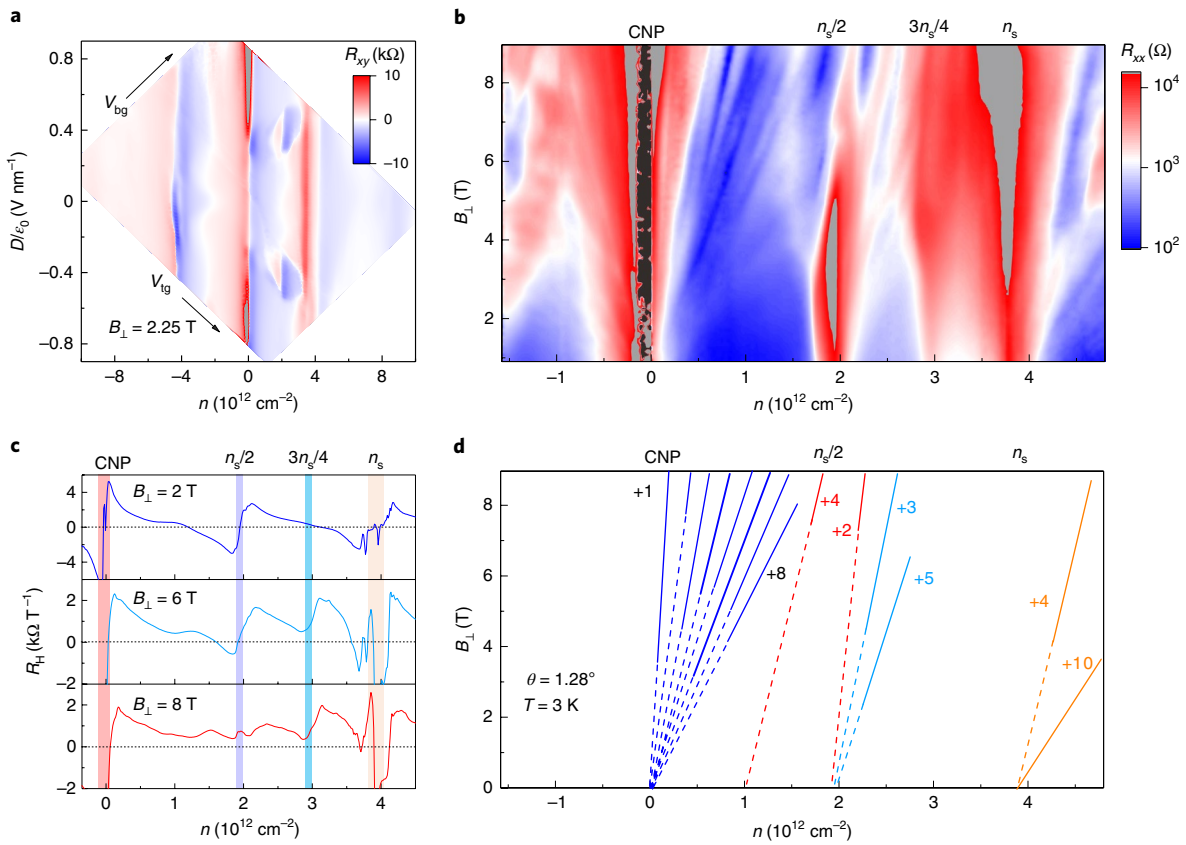


**Fig. 2 | Hall resistances and quantum oscillations.** **a**, Transverse Hall resistance  $R_{xy}$  as a function of carrier density  $n$  and displacement field  $D$  in the  $1.31^\circ$  device with application of a perpendicular magnetic field  $B_{\perp} = 2.25 \text{ T}$ . In this plot, red represents positive  $R_{xy}$  and indicates hole-type Hall carriers, while blue represents negative  $R_{xy}$  and indicates electron-type Hall carriers. **b,d**, Magnetoresistance (Shubnikov-de Haas, SdH) oscillations in the  $1.28^\circ$  device at  $T = 3 \text{ K}$  and with  $B_{\perp}$  varied from  $0.9$  to  $9 \text{ T}$  (**b**). Landau levels are depicted in **d**. In the measurements,  $V_{tg}$  was fixed at  $8 \text{ V}$  and  $V_{bg}$  was swept, producing  $D/\epsilon_0 = -0.45 \text{ V nm}^{-1}$  at half-filling,  $D/\epsilon_0 = -0.35 \text{ V nm}^{-1}$  at  $3/4$  filling and  $D/\epsilon_0 = -0.65 \text{ V nm}^{-1}$  at the CNP. The sweeping trace is marked in Extended Data Fig. 5.  $D$ -fixed sweeping was also performed in the  $1.33^\circ$  device, producing the same Landau levels (LLs) of  $\nu = 3$  and  $\nu = 5$  from half-filling at  $D/\epsilon_0 = -0.4 \text{ V nm}^{-1}$  (Extended Data Fig. 6). **c**, Hall coefficient  $R_H$  ( $R_H = \frac{R_{xy}(B_{\perp}) - R_{xy}(B_{\perp} = 0 \text{ T})}{B_{\perp}}$ ) versus carrier density  $n$  in various perpendicular magnetic fields in the  $1.28^\circ$  device. A sign change at half-filling persists to  $B_{\perp} = 6 \text{ T}$  and disappears at  $B_{\perp} = 8 \text{ T}$ .

gap at half-filling develops only when  $\Delta_{\text{CNP}}$  becomes noticeable. At higher  $D$ , superlattice gap  $\Delta_{\text{ns}}$  closes, leading to a flat conduction band that overlaps with the conduction superlattice bands, with the correlated gap finally vanishing at  $n = n_s/2$  (see Methods and Extended Data Fig. 3). This explanation is also consistent with the observed absence of a correlated gap at  $n = -n_s/2$ , because the small size of the single-particle gap  $\Delta_{\text{ns}}$  and its closing at a smaller  $D$  prevent isolation of the valence flat band due to thermally activated inter-band hopping. The  $D$  response of the correlated gap needs to be explored further, as a higher  $D$  may also broaden the width of the flat band, with effects such as trigonal warping and an overbent sombrero band dispersion in the AB-stacked bilayer graphene. In Extended Data Fig. 3, our calculations indeed show a wider bandwidth when  $D$  is high enough.

In TBG, the flat band is derived intrinsically from strong inter-layer coupling. Under an external displacement field, electrons can be drawn towards the positive gate and repelled from the negative one, inducing an asymmetric distribution of carriers between the top and bottom graphene layers and destroying the expected correlated states, as observed in dual-gated TBG<sup>6</sup>. In TDBG, stronger screening is expected and thus also stronger layer asymmetry under displacement fields. All our devices show half-filling correlated states constrained by unexpected resistive states, which are tuned by a single gate (Fig. 1d and Extended Data Fig. 1). The layer-polarized distribution of electrons abruptly eliminates the correlated gap at  $D$  where

single-particle gaps both at CNP and  $n = n_s$  still persist (Fig. 1d,f). This layer polarization is also reflected by the fact that the correlated state behaves in a less insulating manner at  $D$  where electrons are polarized at the disordered graphene layer (Extended Data Fig. 1).

The half-filling correlated insulating state is further indicated by a sign change in the transverse Hall resistance at  $n = n_s/2$  (Fig. 2a,c). A new Fermi surface originates from the half-filling insulating state and acquires an effective Hall carrier density of  $n_H = n - n_s/2$  (Extended Data Fig. 4). When focusing on doped correlated states, the sign change of the transverse magnetoresistance flanks correlated states, showing electron-like quasiparticles from charge neutrality (correlated insulator) transformed into hole-like quasiparticles from the correlated insulator (superlattice bands). However, in Fig. 2a, the doped domes of the correlated insulator are also constrained by these resistive states, displaying a behaviour distinct from tuning only by Fermi level, thus revealing impacts from layer polarization on doped domes. Moreover, our data also reveal that valence bands are also subject to layer polarization, as shown by single-gated resistive states connecting the gap edges of  $\Delta_{\text{CNP}}$  and  $\Delta_{\text{ns}}$  (Fig. 1d).

The new Fermi surface originating from half-filling correlated states can also be identified by a new set of magneto oscillations that typically serves as a tool to obtain information about the Fermi surface and degeneracy associated with electronic degrees of freedom<sup>2-7</sup>. Figure 2b explicitly shows one-sided Landau levels

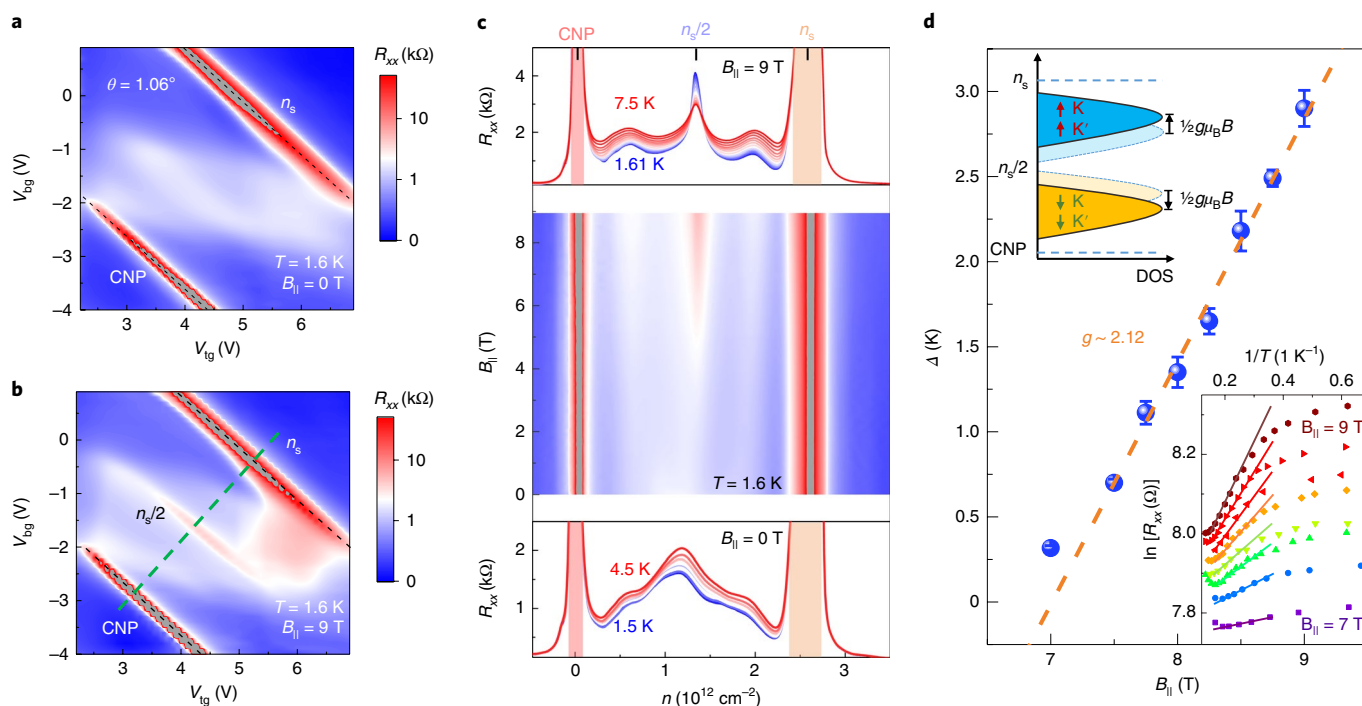


**Fig. 3 | Parallel magnetic-field response of a half-filling correlated insulator.** **a, b**, Resistance colour plot as a function of top and bottom metal gate voltage for the  $1.06^\circ$  device in parallel magnetic fields  $B_{||} = 0$  T (**a**) and  $B_{||} = 9$  T (**b**). The plots in **a**, **b** and **c** share the same colour scale bar. The dark dashed lines in **a** and **b** represent resistive states at the CNP and  $n_s$ . When  $B_{||} = 9$  T is applied, a resistive state appears at  $n_s/2$ . Top- and back-gate voltage sweeping along the green dashed line in **b** keeps  $D/\epsilon_0 = -0.306 \text{ V nm}^{-1}$  and changes  $n$  linearly. **c**, Plot of the resistance at  $D/\epsilon_0 = -0.306 \text{ V nm}^{-1}$ , enhanced by parallel magnetic fields. Insulating behaviour is shown in the top panel when  $B_{||} = 9$  T and  $T < 7.5$  K, but metallic behaviour is shown instead in the bottom panel when  $B_{||} = 0$  T and  $T > 1.5$  K. **d**, Thermal activation gap  $\Delta$  of the  $n_s/2$  insulating state as a function of  $B_{||}$ . A linear fitting, shown as an orange dashed line, gives an effective  $g$  factor of  $\sim 2.12$  according to the Zeeman effect,  $\Delta = g\mu_B B_{||}$ . The gap is extracted by fitting the data with  $R \approx \exp(\Delta/2kT)$  in the bottom inset figure. Top inset: the single-particle flat band is split into upper and lower spin-polarized many-body bands by electron-electron interactions. In parallel magnetic fields, each band contributes to gap broadening by  $g\mu_B B_{||}/2$ . Error bars are estimated from the uncertainty in the range of the simply activated regime.

emanating from half-filling correlated states in a  $1.28^\circ$  device. A Landau level, possibly filling factor  $\nu = 2$ , occurs close to the half-filling correlated insulating state at higher perpendicular field  $B_\perp$ , which is likely to be a signal of the Hofstadter butterfly phenomenon. We present three reasons for this conjecture: (1) this Landau level does not hold down to small  $B_\perp$ ; (2) this Landau level also occurs with the same behaviour when the half-filling correlated insulating state does not exist at larger  $D$  (Extended Data Fig. 5); (3) a fractal Landau level of  $\nu = 4$  and Bloch band filling factor  $s = 1$  also develop at the same range of  $B_\perp$  (here, the Hofstadter energy spectrum is described by the Diophantine formula  $n/n_0 = \nu\phi/\phi_0 + s$ , where  $n_0 = 1/A = n_s/4$ ,  $\phi = B_\perp A$  is the magnetic flux penetrating each moiré unit cell of area  $A$ ,  $\phi_0 = h/e$  is the non-superconducting quantum flux, and  $s = \pm 4$  denotes that Landau fan results from the superlattice band)<sup>24–27</sup>. Two Landau levels with filling factors  $\nu = 3$  and  $\nu = 5$  fanning from the half-filling correlated state are observed. Such a complicated odd-number sequence of Landau levels from a half-filling correlated insulator, together with fractal Landau levels, were checked carefully and were repeated in the  $1.33^\circ$  device (Extended Data Fig. 6; note that the fractal Landau level ( $\nu, s$ ) = (4, 1) seems to be substituted by ( $\nu, s$ ) = (3, 1) in the  $1.33^\circ$  device).

The Landau level filling factors  $\nu = 3$  and  $\nu = 5$  are beyond our expectations given that broken symmetry induces halved filling factors with even numbers for Landau levels resulting from the half-filling correlated insulating state in TBG<sup>5–7</sup>. However, under displacement fields, extra inversion symmetry breaking is introduced, and the Landau fan in Bernal-stacked bilayer graphene could be strongly affected as a consequence<sup>28</sup>. The Landau levels fanning from the CNP in our TDBG devices display a fully lifted degeneracy

in such a displacement field (Fig. 2b). We also found other cases, such as a Landau level of  $\nu = 12$  at a lower  $D$  (Extended Data Fig. 5) or Landau levels of  $\nu = 3$  and  $\nu = 5$  at  $D/\epsilon_0 = -0.4 \text{ V nm}^{-1}$  (Extended Data Fig. 6) dominating the Landau fan diagram from the CNP; these are also beyond the expected fourfold degeneracy, that is, spin and valley without layer degeneracy due to the strong interlayer coupling. Similarly, the halved Landau level filling factor for the half-filling correlated insulating state displays such  $D$ -dependent symmetry breaking.

The half-filling correlated state at  $D/\epsilon_0 = -0.45 \text{ V nm}^{-1}$  persists up to  $B_\perp \approx 7$  T according to the Hall coefficient  $R_H$  behaviour shown in Fig. 2c. Figure 2b and Extended Data Fig. 6 show that the resistance of half-filling starts to increase and then decreases with respect to  $B_\perp$ . We also fitted the gap of the half-filling correlated insulating state in the  $1.33^\circ$  device (Extended Data Fig. 7). This exhibits remarkable enhancement as  $B_\perp$  increases from 0 T to 3 T, then fades substantially at  $B_\perp = 6$  T. Meanwhile, at  $B_\perp = 6$  T, the correlated state at  $3/4n_s$  develops, identified by a resistive state, insulating behaviour and a potential sign change of  $R_H$  (Fig. 2b,c and Extended Data Figs. 6 and 7).

To isolate spin effects from orbital motion, we applied parallel magnetic fields and probed the field dependence of the resistances. Figure 3a shows a vague resistive state but no insulating behaviour at half-filling at  $B_{||} = 0$  T above  $T = 1.6$  K in the device with  $\theta = 1.06^\circ$  (with graphite acting as the back-gate). The parallel magnetic fields monotonously enhance the resistance at  $n = n_s/2$  and lead to an obvious insulating state at moderate  $D$  and higher  $B_{||}$  (Fig. 3b,c). Because  $B_{||}$  only affects the spin degree of freedom, the enhanced insulating behaviour implies that the insulating state at  $n_s/2$  is likely to be



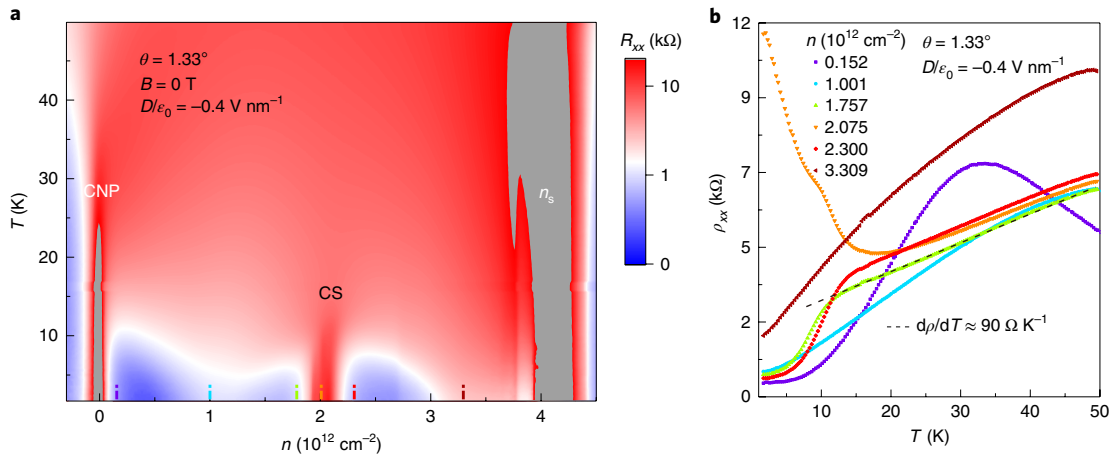


**Fig. 4 | The  $\rho_{xx}$  versus  $T$  behaviour in the  $1.33^\circ$  device. **a**, Four-probe resistance as a function of temperature  $T$  and carrier density  $n$  in the  $1.33^\circ$  device when  $D/\epsilon_0 = -0.4 \text{ V nm}^{-1}$ . The correlated insulating states (CSs) are flanked by two low-resistivity domes. **b**,  $\rho_{xx}$  versus  $T$  curves at various  $n$  plotted with different colours as shown in **a**. A linear fitting of  $\rho_{xx}$ - $T$  at  $n = 1.757 \times 10^{12} \text{ cm}^{-2}$  (dashed line) gives a linearity coefficient of  $d\rho_{xx}/dT = 90 \text{ } \Omega \text{ K}^{-1}$ .**

spin-polarized. Arising from the Zeeman effect, magnetic fields induce gap broadening  $\Delta = g\mu_B B_{\parallel}$  between spin-up and spin-down electrons, where the  $g$  factor for electrons in graphene is  $\sim 2$  and  $\mu_B$  is the Bohr magneton. From the Arrhenius formula of resistance, we obtain a thermal activation gap as a function of  $B_{\parallel}$ , which has a nearly linear relationship (Fig. 3d). Thus, we deduce that the effective  $g$  factor is  $\sim 2.12$ , in agreement with expectations. The possible totally spin-polarized ground state for a half-filling correlated insulator in TDBG makes it reasonable that  $B_{\perp}$  could also first enhance the gap at  $n = n_s/2$  if the spin effect surpasses the orbital effect, in contrast to the case of TBG<sup>4,6</sup>, which shows a decreased gap at half-filling both with  $B_{\parallel}$  and  $B_{\perp}$ .

Note that we also observed a quarter-filling correlated state, formed and enhanced by  $B_{\parallel}$  in the  $1.31^\circ$  device, which is much more sensitive to the displacement field (Extended Data Fig. 8). Compared with the  $1.33^\circ$  device, the  $1.31^\circ$  device shows a much smaller fitted correlated gap due to the stronger disorder, and finally leads to an underestimation of the  $g$  factor,  $g \approx 0.825$ .

Figure 4 presents the  $\rho_{xx}$  versus  $T$  behaviour at various carrier densities with  $D/\epsilon_0 = -0.4 \text{ V nm}^{-1}$  in the  $1.33^\circ$  device, where  $\rho_{xx}$  is the four-probe resistivity. In proximity to the half-filling state, the resistivity shows an abrupt dropping-down onset at  $T \approx 12 \text{ K}$  and is linearly reduced at higher temperatures, which is very distinct from states at carrier density far away from  $n = n_s/2$  (Fig. 4b). This  $\rho_{xx}$ - $T$  behaviour observed in TBG and ABC-stacked trilayer graphene is a signature of superconductivity<sup>5-7,21</sup>. The linear relationship between  $\rho_{xx}$  and  $T$  observed in TBG is likely to support electron-phonon scattering or strange metal behaviour, but this is still under debate<sup>16,29</sup>. In our TDBG  $1.33^\circ$  device, the linearity coefficient of  $d\rho_{xx}/dT$  for  $n = 1.757 \times 10^{12} \text{ cm}^{-2}$  and  $n = 2.3 \times 10^{12} \text{ cm}^{-2}$  is  $\sim 90 \text{ } \Omega \text{ K}^{-1}$ , and a small saturated resistivity of  $\sim 400 \text{ } \Omega$  persists at the lowest temperature of  $\sim 1.5 \text{ K}$ . Multi-probe measurements suggest that this device is actually composed of a majority of  $\theta \approx 1.33^\circ$  and a minority of  $\theta \approx 1.1^\circ$  in series (Extended Data Fig. 9). The twist-angle inhomogeneity is probably the reason why the resistance cannot reach zero in this device. We did observe zero resistance in the  $1.28^\circ$  device (Extended Data Fig. 10), but more measurements are required to verify the presence of superconductivity at the doped correlated insulating state in TDBG.

Our work demonstrates electrically tunable correlated states in TDBG. The hypothesized spin-polarized ground state at half-filling, different from that in TBG, reveals the important role played by the layer numbers of the original constituent two-dimensional (2D)

materials in the twist system. Electronic states, for example, in the electrically tunable ferromagnetic Mott insulator<sup>30</sup>, Chern bands<sup>15</sup> and spin-triplet topological superconductivity<sup>31</sup>, are potentially present in TDBG and call for further theoretical and experimental<sup>32,33</sup> efforts to reveal the underlying mechanism.

### Online content

Any methods, additional references, Nature Research reporting summaries, source data, extended data, supplementary information, acknowledgements, peer review information; details of author contributions and competing interests; and statements of data and code availability are available at <https://doi.org/10.1038/s41567-020-0825-9>.

Received: 30 October 2019; Accepted: 5 February 2020;  
Published online: 30 March 2020

### References

1. Bistritzer, R. & MacDonald, A. H. Moiré bands in twisted double layer graphene. *Proc. Natl Acad. Sci. USA* **108**, 12233–12237 (2011).
2. Cao, Y. et al. Superlattice-induced insulating states and valley-protected orbits in twisted bilayer graphene. *Phys. Rev. Lett.* **117**, 116804 (2016).
3. Kim, K. et al. Tunable moiré bands and strong correlations in small twist angle bilayer graphene. *Proc. Natl Acad. Sci. USA* **114**, 3364–3369 (2017).
4. Cao, Y. et al. Correlated insulator behaviour at half-filling in magic-angle graphene superlattices. *Nature* **556**, 80–84 (2018).
5. Cao, Y. et al. Unconventional superconductivity in magic-angle graphene superlattices. *Nature* **556**, 43–50 (2018).
6. Yankowitz, M. et al. Tuning superconductivity in twisted bilayer graphene. *Science* **363**, 1059–1064 (2019).
7. Lu, X. et al. Superconductors, orbital magnets and correlated states in magic-angle bilayer graphene. *Nature* **574**, 653–657 (2019).
8. Castro Neto, A. H., Guinea, F., Peres, N. M. R., Novoselov, K. S. & Geim, A. K. The electronic properties of graphene. *Rev. Mod. Phys.* **81**, 109–162 (2009).
9. Zhang, Y. et al. Direct observation of a widely tunable bandgap in bilayer graphene. *Nature* **459**, 820–823 (2009).
10. Castro, E. V. et al. Biased bilayer graphene: semiconductor with a gap tunable by the electric field effect. *Rev. Phys. Lett.* **99**, 216802 (2007).
11. Zhang, Y.-H., Mao, D., Cao, Y., Jarillo-Herrero, P. & Senthil, T. Nearly flat Chern bands. *Phys. Rev. B* **99**, 075127 (2019).
12. Sharpe, A. L. et al. Emergent ferromagnetism near three-quarters fillings in twisted bilayer graphene. *Science* **365**, 605–608 (2019).
13. Serlin, M. et al. Intrinsic quantized anomalous Hall effect in a moiré heterostructure. *Science* **367**, 900–903 (2020).
14. Xu, C. & Balents, L. Topological superconductivity in twisted multilayer graphene. *Phys. Rev. Lett.* **121**, 087001 (2018).

15. Po, H. C., Watanabe, H. & Vishwanath, A. Fragile topology and Wannier obstructions. *Phys. Rev. Lett.* **121**, 126402 (2018).
16. Cao, Y. et al. Strange metal in magic-angle graphene with near Planckian dissipation. *Phys. Rev. Lett.* **124**, 076801 (2020).
17. Liu, C.-C., Zhang, L.-D., Chen, W.-Q. & Yang, F. Chiral spin density wave and  $d+id$  superconductivity in the magic-angle-twisted bilayer graphene. *Phys. Rev. Lett.* **121**, 217001 (2018).
18. Koshino, M. et al. Maximally localized Wannier orbitals and the extended Hubbard model for twisted bilayer graphene. *Phys. Rev. X* **8**, 031087 (2018).
19. Po, H. C., Zou, L., Vishwanath, A. & Senthil, T. Origin of Mott insulating behavior and superconductivity in twisted bilayer graphene. *Phys. Rev. X* **8**, 031089 (2018).
20. Chen, G. et al. Evidence of a gate-tunable Mott insulator in trilayer graphene moiré superlattice. *Nat. Phys.* **15**, 237–241 (2019).
21. Chen, G. et al. Signatures of gate-tunable superconductivity in trilayer graphene/boron nitride moiré superlattice. *Nature* **572**, 215–219 (2019).
22. Chen, G. et al. Tunable correlated Chern insulator and ferromagnetism in a moiré superlattice. *Nature* **579**, 56–61 (2020).
23. Li, Z. Q. et al. Band structure asymmetry of bilayer graphene revealed by infrared spectroscopy. *Phys. Rev. Lett.* **102**, 037403 (2009).
24. Dean, C. R. et al. Hofstadter's butterfly and the fractal quantum Hall effect in moiré superlattices. *Nature* **497**, 598–602 (2013).
25. Ponomarenko, L. A. et al. Cloning of Dirac fermions in graphene superlattices. *Nature* **497**, 594–597 (2013).
26. Hunt, B. et al. Massive Dirac fermions and Hofstadter butterfly in a van der Waals heterostructure. *Science* **340**, 1427–1430 (2013).
27. Yang, W. et al. Epitaxial growth of single-domain graphene on hexagonal boron nitride. *Nat. Mater.* **12**, 792–797 (2013).
28. Maher, P. et al. Tunable fractional quantum Hall phases in bilayer graphene. *Science* **345**, 61–64 (2014).
29. Polshyn, H. et al. Large linear-in-temperature resistivity in twisted bilayer graphene. *Nat. Phys.* **15**, 1011–1016 (2019).
30. Erickson, A. S. et al. Ferromagnetism in the Mott insulator  $\text{Ba}_2\text{NaOsO}_6$ . *Phys. Rev. Lett.* **99**, 016404 (2007).
31. Lee, J. Y. et al. Theory of correlated insulating behavior and spin-triplet superconductivity in twisted double bilayer graphene. *Nat. Commun.* **10**, 5333 (2019).
32. Liu, X. et al. Spin-polarized correlated insulator and superconductor in twisted double bilayer graphene. Preprint at <https://arxiv.org/pdf/1903.08130.pdf> (2019).
33. Cao, Y. et al. Electric field tunable correlated states and magnetic phase transitions in twisted bilayer–bilayer graphene. Preprint at <https://arxiv.org/pdf/1903.08596.pdf> (2019).

**Publisher's note** Springer Nature remains neutral with regard to jurisdictional claims in published maps and institutional affiliations.

© The Author(s), under exclusive licence to Springer Nature Limited 2020

## Methods

**Device fabrication.** The TDBG devices were fabricated following a typical ‘tear and stack’ technique<sup>34</sup>. Raw materials of bilayer graphene, hBN (20–35 nm thick) and graphite flakes were first exfoliated on SiO<sub>2</sub> (300 nm thick), then annealed in an Ar/H<sub>2</sub> mixture at temperature up to 450 °C. Usually, moderate H<sub>2</sub> plasma etching was also applied to fully get rid of contaminations arising from the exfoliation process. We used poly(bisphenol A carbonate) (PC) supported by polydimethylsiloxane (PDMS) on a glass slide to first pick up hBN and then tear and pick up bilayer graphene. A home-made micro-position stage was used to control the rotation angle with an error range of 0.1°. We performed no annealing on TDBG as it tends to relax to a twist angle of nearly  $\theta=0^\circ$  once the temperature is high. The fabrication of the metal top-gate and electrodes followed a standard electron-beam lithography process and electron-beam metal evaporation. The devices were designed as a Hall bar structure and shaped by traditional reactive ion etching with a CHF<sub>3</sub> and O<sub>2</sub> gas mixture. The metal top-gate also acted as a mask for etching to ensure that the channel was fully gated. Finally, all the bars were contacted via a 1D edge contact with Cr/Au electrodes<sup>35</sup>.

**Transport measurements.** Transport measurements were performed in cryostat with a base temperature of 1.5 K. We applied standard lock-in techniques to measure the resistance, with 31 Hz excitation frequency and 1 nA alternating excitation current or less than 200  $\mu$ V alternating excitation bias voltage, achieved by a 1/1,000 voltage divider. All the transport data were acquired by four-terminal measurements.

**Twist angle extraction.** A large range of twist angle was achieved in our TDBG devices. Note that the encapsulated structure prevents the use of traditional probe-characterizing methods to detect twist angle  $\theta$ , and we have to extract  $\theta$  from transport data acquired at cryogenic temperatures. Before being loaded in a cryostat, devices were first picked at room temperature. The flat band present in a magic-angle twisted graphene superlattice greatly lowers the carrier mobility, causing CNP to be unrecognized in  $R-V_g$  or  $G-V_g$  curves, which have a ‘U’ rather than ‘V’ shape at room temperature.

For a small  $\theta$ , the calculation of  $\theta$  follows the formula

$$A = \frac{4}{n_s} = \frac{\sqrt{3}}{2} \lambda^2 \approx \frac{\sqrt{3} a^2}{2\theta^2}$$

where  $A$  is the moiré unit cell area,  $\lambda$  is the moiré wave length,  $a=0.246$  nm is the lattice constant of graphene and  $n_s$  is the carrier density at which the flat conduction band is fulfilled. Generally, in TDBG, we still follow the view that four electrons or holes in a moiré unit cell fill the first conduction or valence band for four-fold spin and valley degeneracy, yielding single-particle superlattice gaps. In most cases, estimating  $\theta$  through  $n_s$  has some degree of error, because superlattice gaps are usually present over a range of  $n_s$ . Instead, we tend to determine  $\theta$  via the carrier density  $n_s/2$  for the half-filling correlated insulating state. In devices with well-developed quantum oscillations, an alternative is to obtain the moiré unit cell area directly through Landau level crossing at magnetic flux  $\phi=B_\perp A=\phi_0/q$ , where  $B_\perp$  is perpendicular magnetic field,  $q$  is an integer and  $\phi_0=h/e$  is the non-superconductivity magnetic flux.

**Insulating states in devices with various twist angles.** The half-filling correlated state has been observed in our devices with  $\theta$  ranging from 0.98° to 1.33° (Extended Data Fig. 1). Note that in devices with  $\theta=0.98^\circ$  and  $\theta=1.06^\circ$ , vague resistance peaks, but without insulating behaviour, develop at half-filling above  $T=1.6$  K (see also Fig. 3a). However, in strong in-plane magnetic fields, these two devices can develop insulating behaviour at half-filling above  $T=1.6$  K (Fig. 3c). For 1.26°, 1.28° and 1.33° devices, on altering the direction of the displacement fields, the half-filling correlated state shows different resistance, which is considered a sign of layer asymmetry in the carrier distribution. Interestingly, the superlattice gap  $\Delta_{ns}$  at  $n=-n_s$  exhibits ‘reentrant’ behaviour as the displacement field  $D$  is tuned over a large range; that is, the strengthening of  $D$  first switches this gap off and then switches it on. Moreover, single-particle gaps occur at  $\pm 3n_s$ , where 12 electrons or holes fill a moiré unit cell. Such a phenomenon resembles the case of high-order superlattice gaps in a graphene/hBN superlattice<sup>36</sup> and is consistent with our calculation results (Extended Data Fig. 3).

**Single-particle gaps tuned by displacement fields in the 0.98° device.** We measured single-particle gaps in the 0.98° device with respect to displacement fields  $D$  at  $n=0$  ( $\Delta_{\text{CNP}}$ ),  $n=\pm n_s$  ( $\Delta_{ns}$  and  $\Delta_{-ns}$ ) and  $n=\pm 3n_s$  ( $\Delta_{3ns}$  and  $\Delta_{-3ns}$ ). All single-particle superlattice gaps reach their highest values at  $D/\epsilon_0=0$  and then decrease in displacement fields. For  $|D|/\epsilon_0 \approx 0.3\text{--}0.5$  V nm<sup>-1</sup>, which is the interval where the half-filling insulating states can be observed in devices with  $\theta \approx 1.2\text{--}1.3^\circ$ ,  $\Delta_{ns}$  and  $\Delta_{-ns}$  drop to zero or nearly zero, preventing isolation of the first conduction and valence bands. The coexistence of  $\Delta_{ns}$  and  $\Delta_{\text{CNP}}$  only occurs in a narrow range of  $D$  and, within this range, both  $\Delta_{ns}$  and  $\Delta_{\text{CNP}}$  have low values. Small neighbour single-particle gaps at an angle such as  $\theta=0.98^\circ$  make thermally activated interband hopping considerable at our base temperature and contribute to the absence of insulating behaviour for the half-filled conduction band. The data acquired in the 0.98° device reveal the importance of neighbour

single-particle gaps in a correlated insulator. In addition,  $\Delta_{ns}$  appears again at  $|D|/\epsilon_0 > 0.5$  V nm<sup>-1</sup>, providing the possibility of well-isolated flat valence band formation at high  $D$ .

**Band structure calculations.** We used the extended tight-binding model to calculate the band structures of the twisted double bilayer graphene. Extended Data Fig. 3 shows the evolution of band structure as the displacement field is increased. As well as the isolated flat conduction band and evolution of single-particle gaps at the CNP and  $\pm n_s$ , which are consistent with our experimental observations, the calculated results also provide information about the relationship between the bandwidth of the isolated conduction band and  $D$ . When  $D$  is high enough, the calculated bandwidth becomes so large ( $>20$  meV) that it is comparable to the on-site Coulomb repulsion energy and thus probably leads to the absence of a correlated insulating state.

In our calculations, the atomic positions of TDBG are fully relaxed with the classical force-field approach implemented in the LAMMPS package<sup>37</sup>. The second-generation REBO potential<sup>38</sup> and Kolmogorov–Crespi (KC) potential<sup>39</sup> were used to describe the intra-layer and inter-layer interactions. Only the  $p_z$  orbital of the carbon atom is considered in our tight-binding model,  $H = \sum_i \epsilon_i a_i^\dagger a_i + \sum_{ij} V_{ij} a_i^\dagger a_j$ , where  $a_i^\dagger$ ,  $a_i$  are the creation and annihilation operators.  $V_{ij} = V_{pp\sigma} \sin^2 \theta + V_{pp\pi} \cos^2 \theta$ , where  $\theta$  is the angle between the orbital axes and  $R_{ij} = R_i - R_j$  connects the two orbital centres.  $\theta = \pi/2$  ( $\theta=0$ ) corresponds to the pair of atoms in the same layer (a pair of atoms on top of each other). The Slater–Koster<sup>40</sup> parameters,  $V_{pp\pi}$  and  $V_{pp\sigma}$ , depend on the distance  $r$  between two orbitals as  $V_{pp\sigma}(r) = V_{pp\sigma}^0 e^{q_\sigma(1-\frac{r}{l_c})} F_c(r)$  and  $V_{pp\pi}(r) = V_{pp\pi}^0 e^{q_\pi(1-\frac{r}{l_c})} F_c(r)$  (ref. 41). In our calculation, we use  $V_{pp\pi}^0 = -2.81$  eV,  $V_{pp\sigma}^0 = 0.48$  eV,  $a_\sigma = 3.349$  Å,  $q_\sigma = 7.428$ ,  $a_\pi = 1.418$  Å,  $q_\pi = 3.1451$ ,  $F_c(r) = (1 + e^{(r-l_c)/l_c})^{-1}$ ,  $l_c = 0.265$  Å and  $r_c = 6.165$  Å (ref. 42). The electric field is added through the onsite energy  $\epsilon_i = Ez_i$ , where  $E$  is the strength of the electric field and  $z_i$  is the atomic  $z$ -axis coordinate. The band structures were obtained with the WannierTools open-source software package<sup>43</sup>.

**Quantum oscillations.** We repeatedly observed magnetoresistance (SdH) oscillations near half-filling in the 1.33° device. Extended Data Fig. 6 shows the same Landau levels with filling factors  $\nu=3$  and  $\nu=5$  originating from the half-filling correlated state. The differences between oscillation features shown in Fig. 2b for the 1.28° device and Extended Data Fig. 6 for the 1.33° device are from the Landau level structures around the CNP and Hofstadter butterfly patterns. In Extended Data Fig. 6, Landau levels near the CNP show dominant filling factors  $\nu=3$  and  $\nu=5$  and weaker  $\nu=4$ , possibly because of a weaker displacement field compared with that in Fig. 2b. The Hofstadter butterfly in Extended Data Fig. 6 is established by a series of fractal Landau levels,  $(\nu, s) = (3, 1)$ ,  $(2, 2)$ ,  $(1, 3)$  and  $(2, 3)$  ( $\nu$  and  $s$  have the same meanings as in the main text). The fractal Landau level  $(\nu, s) = (3, 1)$  in Extended Data Fig. 6 is replaced by  $(\nu, s) = (4, 1)$  in Fig. 2b.

The Landau level structure is affected by displacement field  $D$ . In a weaker  $D$ , Landau levels from the CNP show four-fold degeneracy on the hole branch and dominant  $\nu=12$  on the electron branch (Extended Data Fig. 5c). In a larger  $D$ , degeneracy is fully lifted. For the Hofstadter butterfly, similarly, a larger  $D$  induces more visible fractal Landau levels (displayed in Extended Data Fig. 5e) than in a weaker field, in which only Landau level crossings and unrecognized fractal Landau levels are developed.

## Quarter-filling correlated insulating state induced by parallel magnetic fields.

The in-plane magnetic field strengthens the half-filling insulator and also induces a quarter-filling correlated insulating state, as shown in Extended Data Fig. 8 for the 1.31° device. Stronger disorder in the 1.31° device leads to an underestimation of the thermal activation gap and finally a fitted  $g$  factor of less than 2. Similarly, the inability to observe a  $B_\parallel$ -induced spin-polarized 3/4-filling correlated state could also be attributed to the 1.31° device being of bad quality.

## Data availability

The data represented in Figs. 1c–f, 2a–c, 3a–d and 4 are provided with the paper as Source Data. All other data that support the plots within this paper and other findings of this study are available from the corresponding author upon reasonable request.

## References

- Kim, K. et al. Van der Waals heterostructures with high accuracy rotational alignment. *Nano Lett.* **16**, 1989–1995 (2016).
- Wang, L. et al. One-dimensional electrical contact to a two-dimensional material. *Science* **342**, 614–617 (2013).
- Chen, G. et al. Emergence of tertiary Dirac points in graphene moiré superlattices. *Nano Lett.* **6**, 3576–3581 (2017).
- LAMMPS molecular dynamics simulator (Sandia National Laboratories, 2020); <http://lammps.sandia.gov/>
- Brenner, D. W. et al. A second-generation reactive empirical bond order (REBO) potential energy expression for hydrocarbons. *J. Phys. Condens. Matter* **14**, 783–802 (2002).

39. Kolmogorov, A. N. & Crespi, V. H. Registry-dependent interlayer potential for graphitic systems. *Phys. Rev. B* **71**, 235415 (2005).
40. Slater, J. C. & Koster, G. F. Simplified LCAO method for the periodic potential problem. *Phys. Rev.* **94**, 1498 (1954).
41. Trambly de Laissardi re, G., Mayou, D. & Magaud, L. Numerical studies of confined states in rotated bilayers of graphene. *Phys. Rev. B* **86**, 125413 (2012).
42. Haddadi, F., Wu, Q., Kruchkov, A. J. & Yazyev, O. V. Moir  flat bands in twisted double bilayer graphene. *Nano Lett.* <https://doi.org/10.1021/acs.nanolett.9b05117> (2020).
43. Wu, Q., Zhang, S., Song, H.-F., Troyer, M. & Soluyanov, A. A. WannierTools: an open-source software package for novel topological materials. *Comput. Phys. Commun.* **224**, 405–416 (2018).

## Acknowledgements

We appreciate helpful discussions with G. Chen at UC Berkeley, G. Pan and S. Li at the Institute of Physics (IOP), Chinese Academy of Sciences (CAS) and also help with transport measurements from F. Gao and Y. Li at IOP, CAS. G.Z. is grateful for financial support from NSFC (grants nos. 11834017 and 61888102), the Strategic Priority Research Program of CAS (grant no. XDB30000000), the Key Research Program of Frontier Sciences of CAS (grant no. QYZDB-SSW-SLH004) and the National Key R&D program (grant no. 2016YFA0300904). Q.W. and O.V.Y. acknowledge support from NCCR MARVEL. Z.Y.M. acknowledges support from the National Key R&D Program (2016YFA0300502), the Strategic Priority Research Program of CAS (XDB28000000), the NSFC (11574359) and the Research Grants Council of Hong Kong Special Administrative Region of China (17303019). K.W. and T.T. acknowledge support from

the Elemental Strategy Initiative conducted by the MEXT, Japan, A3 Foresight by JSPS and the CREST (JPMJCR15F3), JST. Numerical calculations were performed at the Swiss National Supercomputing Center (CSCS) under project no. s832, the facilities of Scientific IT and Application Support Center of EPFL, the Center for Quantum Simulation Sciences in the Institute of Physics, Chinese Academy of Sciences, the Computational Initiative of the Faculty of Science at the University of Hong Kong and the Platform for Data-Driven Computational Materials Discovery at the Songshan Lake Materials Laboratory, Guangdong, China.

## Author contributions

G.Z. supervised the work and C.S. conceived the project. C.S. and Y.C. fabricated the devices. C.S. performed the transport measurements and data analysis. Q.W. and O.V.Y. carried out numerical calculations. K.W. and T.T. provided hBN crystals. C.S., Z.Y.M. and G.Z. wrote the paper. All other authors were involved in discussions of this work.

## Competing interests

The authors declare no competing interests.

## Additional information

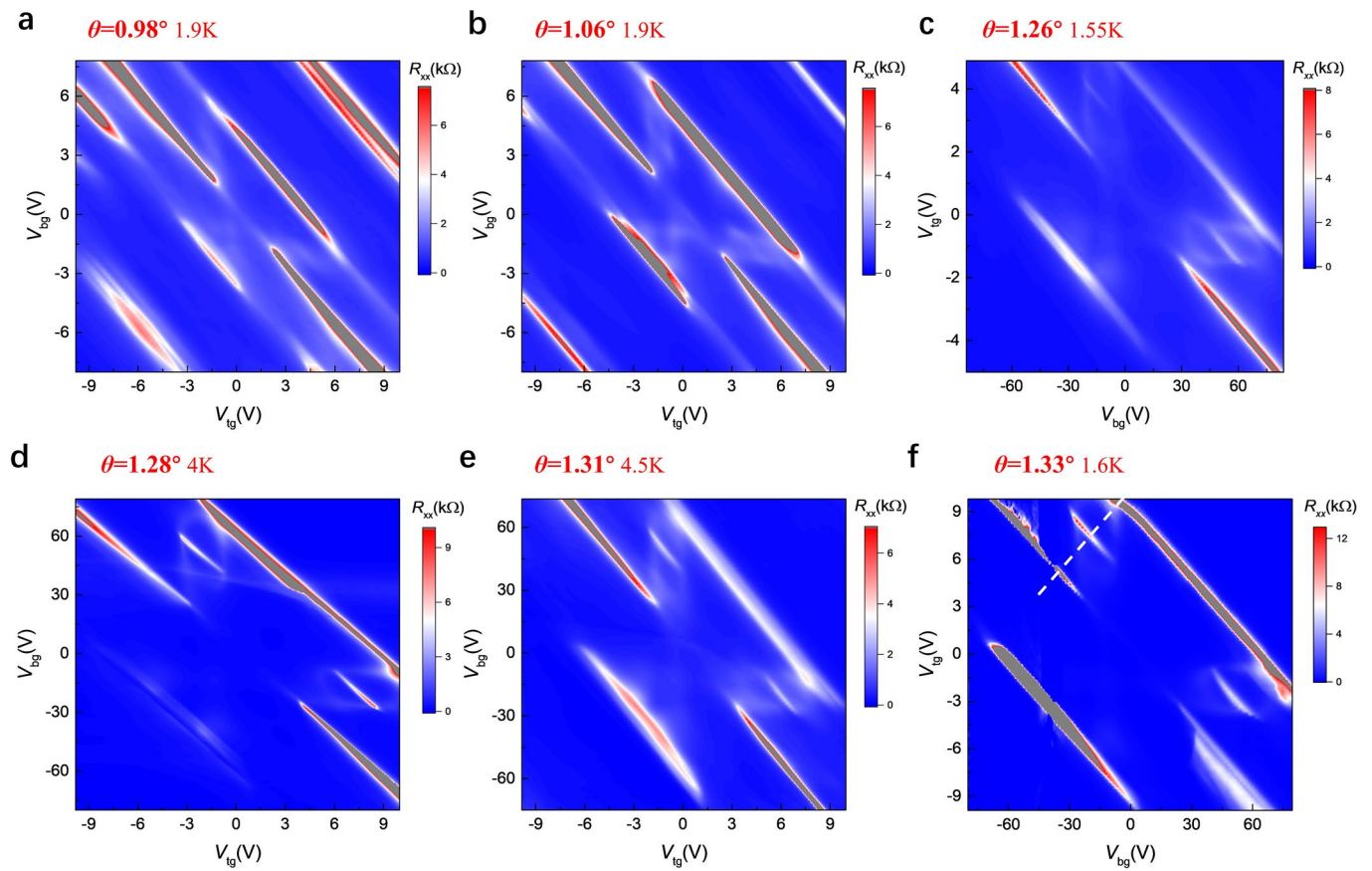
**Extended data** is available for this paper at <https://doi.org/10.1038/s41567-020-0825-9>.

**Supplementary information** is available for this paper at <https://doi.org/10.1038/s41567-020-0825-9>.

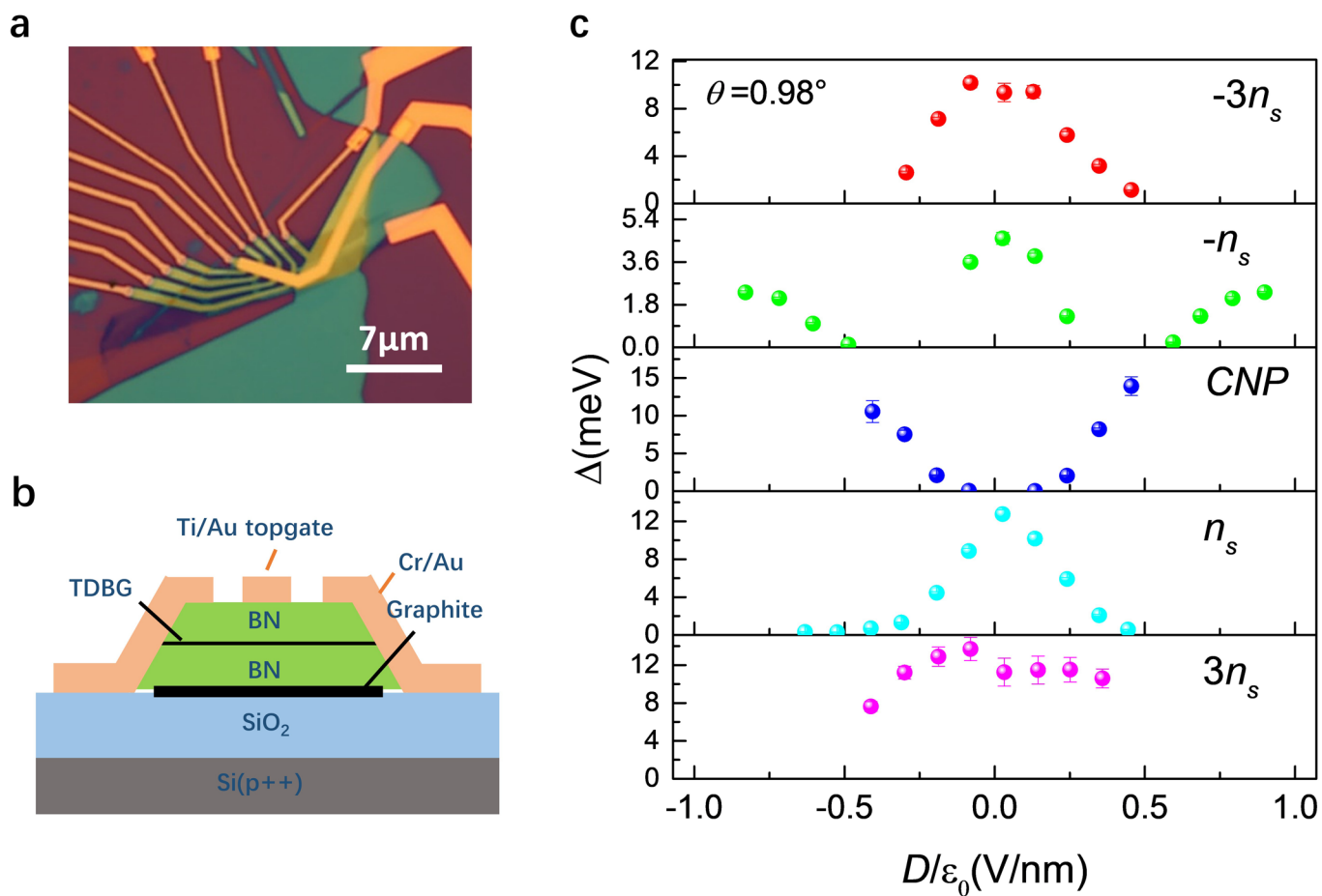
**Correspondence and requests for materials** should be addressed to G.Z.

**Reprints and permissions information** is available at [www.nature.com/reprints](http://www.nature.com/reprints).

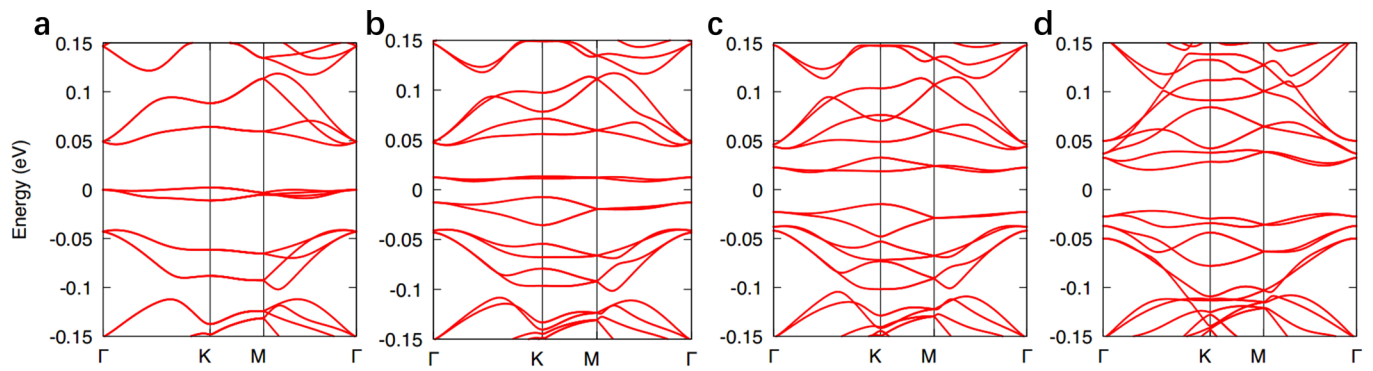




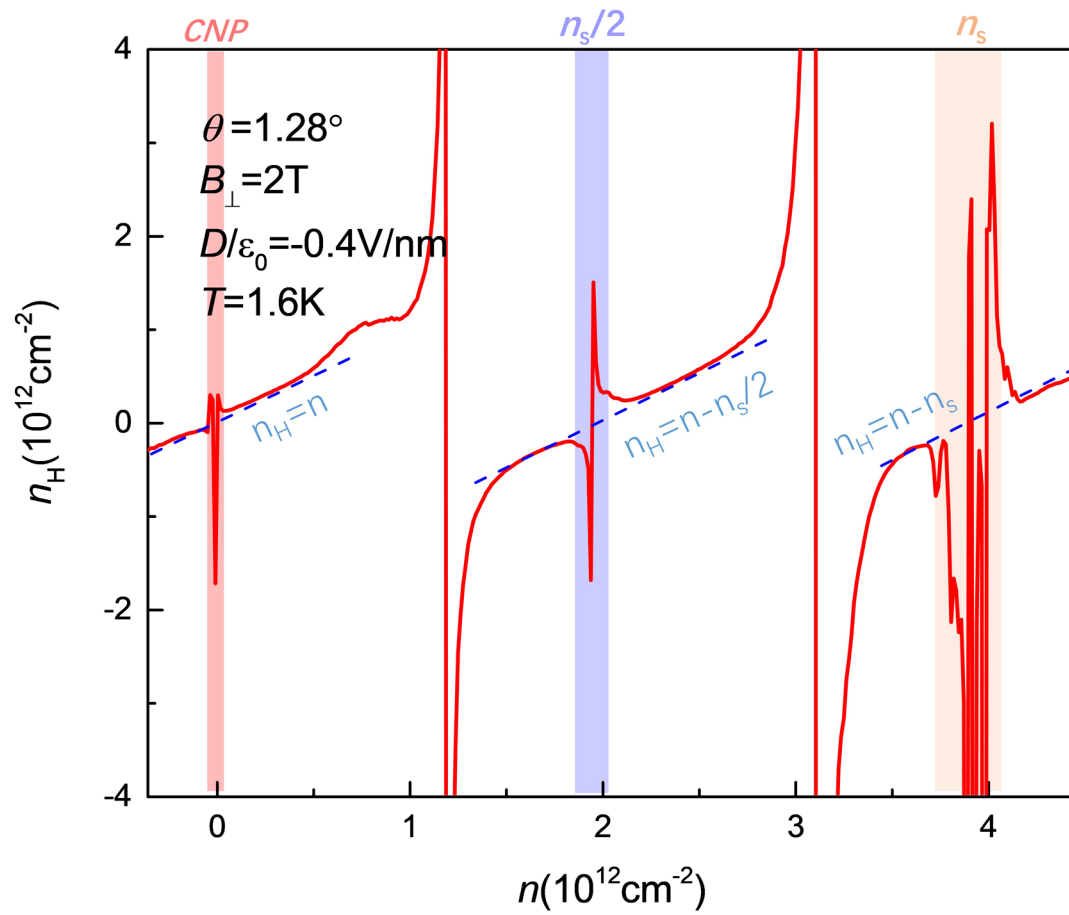
**Extended Data Fig. 1 | Resistance mapping plots of all devices.** The resistance is plotted as a function of top and back gate voltages. Devices in our studies varies from  $0.98^\circ$  to  $1.33^\circ$ . The white dash line in **f** marks  $D/\epsilon_0 = -0.4\text{V/nm}$ .



**Extended Data Fig. 2 | Single-particle band gaps in the 0.98°-device.** **a**, Optical microscope image of the 0.98°-device. **b**, Schematic of device structure. **c**, Single-particle gaps at  $n=0$ ,  $n=\pm n_s$  and  $n=\pm 3n_s$  with respect to displacement field. The thermal-activation gaps are fitted with Arrhenius formula  $R\text{-exp}(\Delta/2kT)$ . Error bars are estimated from the uncertainty in the range of simply activated regime.

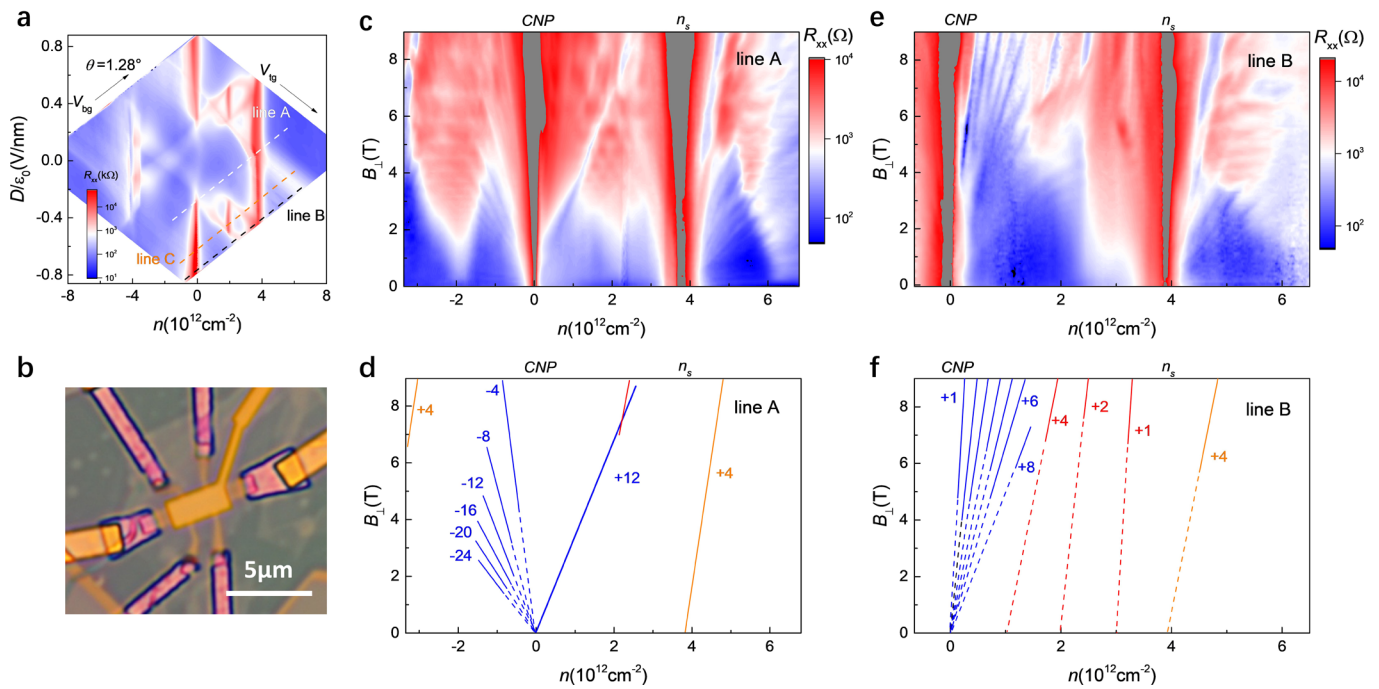


**Extended Data Fig. 3 | Calculated band structures of 1.3° twisted double bilayer graphene in various displacement fields.** The electric fields (and corresponding displacement fields calculated with the relative dielectric constant of *h*BN) in **a**, **b**, **c** and **d** are 0,  $|E|=50\text{mV/nm}$  ( $|D|/\epsilon_0\approx 0.2\text{V/nm}$ ),  $|E|=90\text{mV/nm}$  ( $|D|/\epsilon_0\approx 0.36\text{V/nm}$ ) and  $|E|=200\text{mV/nm}$  ( $|D|/\epsilon_0\approx 0.8\text{V/nm}$ ), respectively. Because of ignoring screening effects in TDBG, the calculated regime of displacement field to produce isolated flat band would be relatively lower than experimental results. In our calculations, energies are shifted such that CNP is located at zero energy.

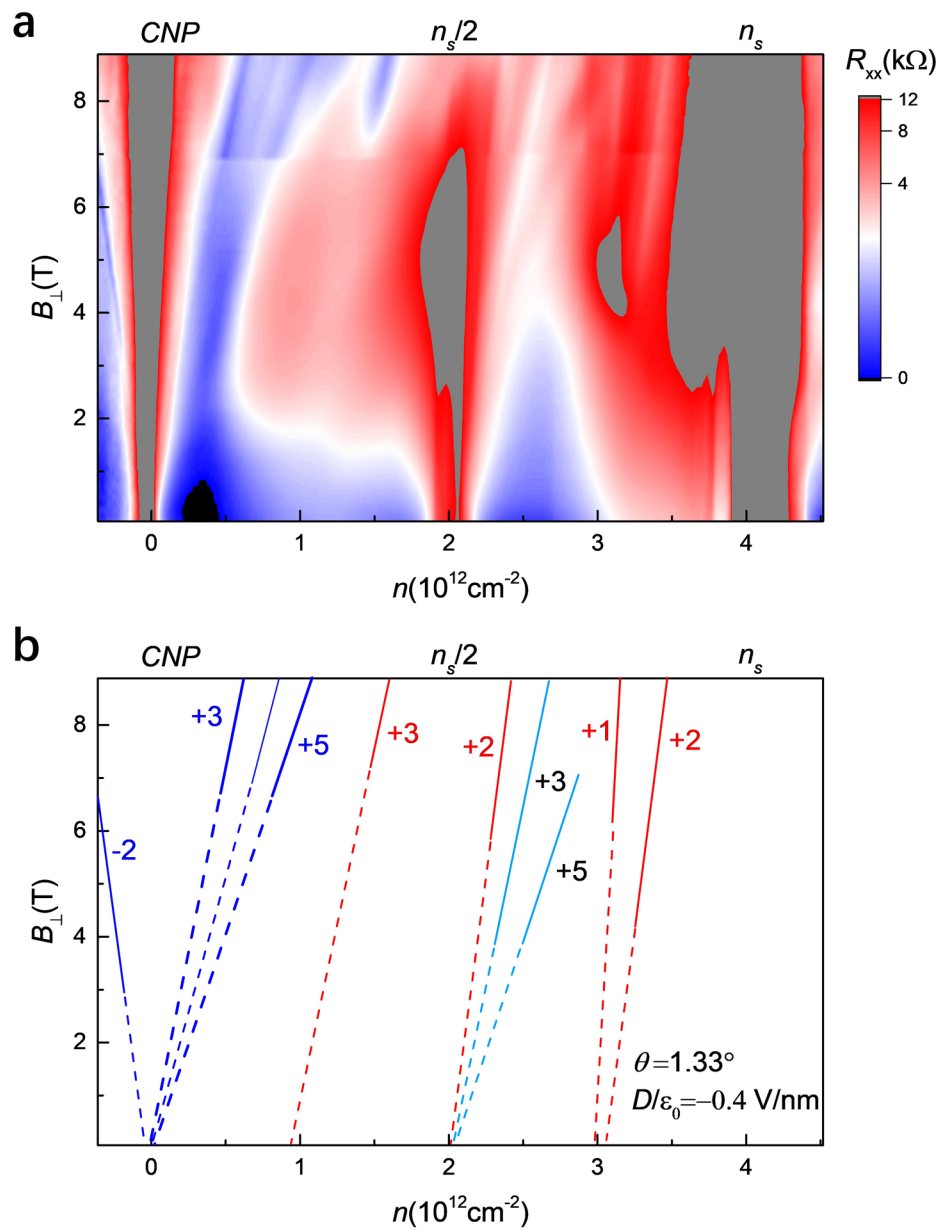


**Extended Data Fig. 4 | Hall carrier density measurements in the  $1.28^\circ$ -device.** The Hall carrier density  $n_H = -1/(eR_H)$  in the  $1.28^\circ$ -device is plotted as a function of gate-induced charge density. The data are acquired at magnetic field  $B_\perp = 2\text{T}$  and  $D/\epsilon_0 = -0.4\text{V/nm}$ . Vertical colored bars correspond to various fillings of flat conduction band. The Hall carrier density switches types of Hall carriers at  $n=0$ ,  $n=n_s/2$  and  $n=n_s$ , and strictly follows  $n_H=n$ ,  $n_H=n-n_s/2$  and  $n_H=n-n_s$  in the vicinity of correspondingly empty, half and full filling of flat conduction band. This behavior serves a definitely evidence of fully opened gap at half filling.

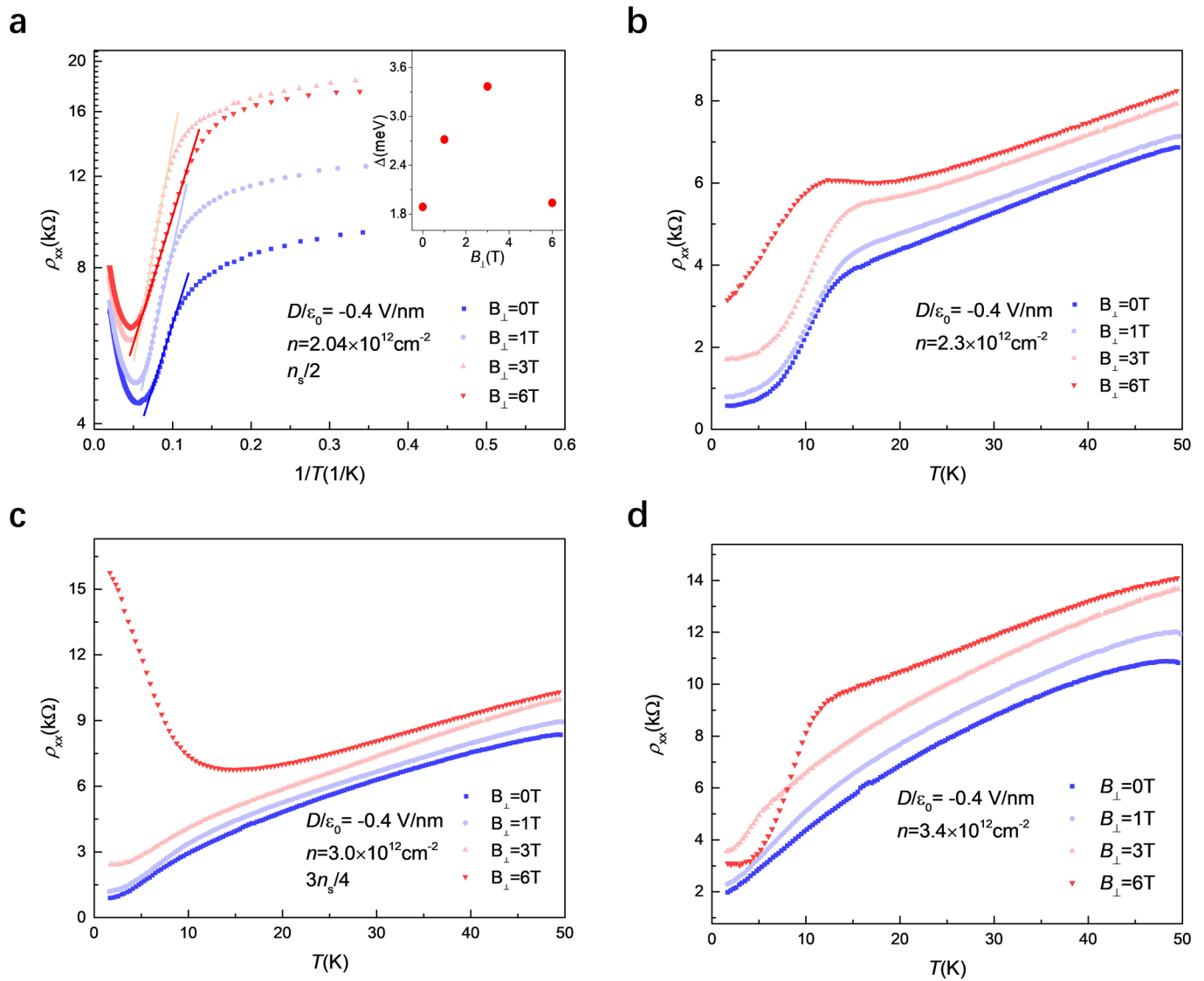




**Extended Data Fig. 5 | Quantum oscillations in the absence of half-filling correlated state in the 1.28°-device.** **a**, Transformed resistance mapping plot from Fig. 1d as a function of  $n$  and  $D$ . Line A, B and C denote the corresponding gate sweeping traces. Line C is the sweeping trace for Fig. 2b. **b**, Optical microscope picture of the 1.28°-device. **c**, **e**, Magneto resistance vs. carrier density  $n$  in perpendicular magnetic field  $B_{\perp}$  with gate voltage swept along trace A and B, respectively. At the same density, displacement field in **e** is always stronger than **c**. **d**, **f**, Schematic diagram of Landau levels observed in **c** and **e**, respectively. Landau levels originated from CNP and superlattice band edge are plotted with blue and orange colors, respectively. Fractal Landau levels are plotted with red colors.



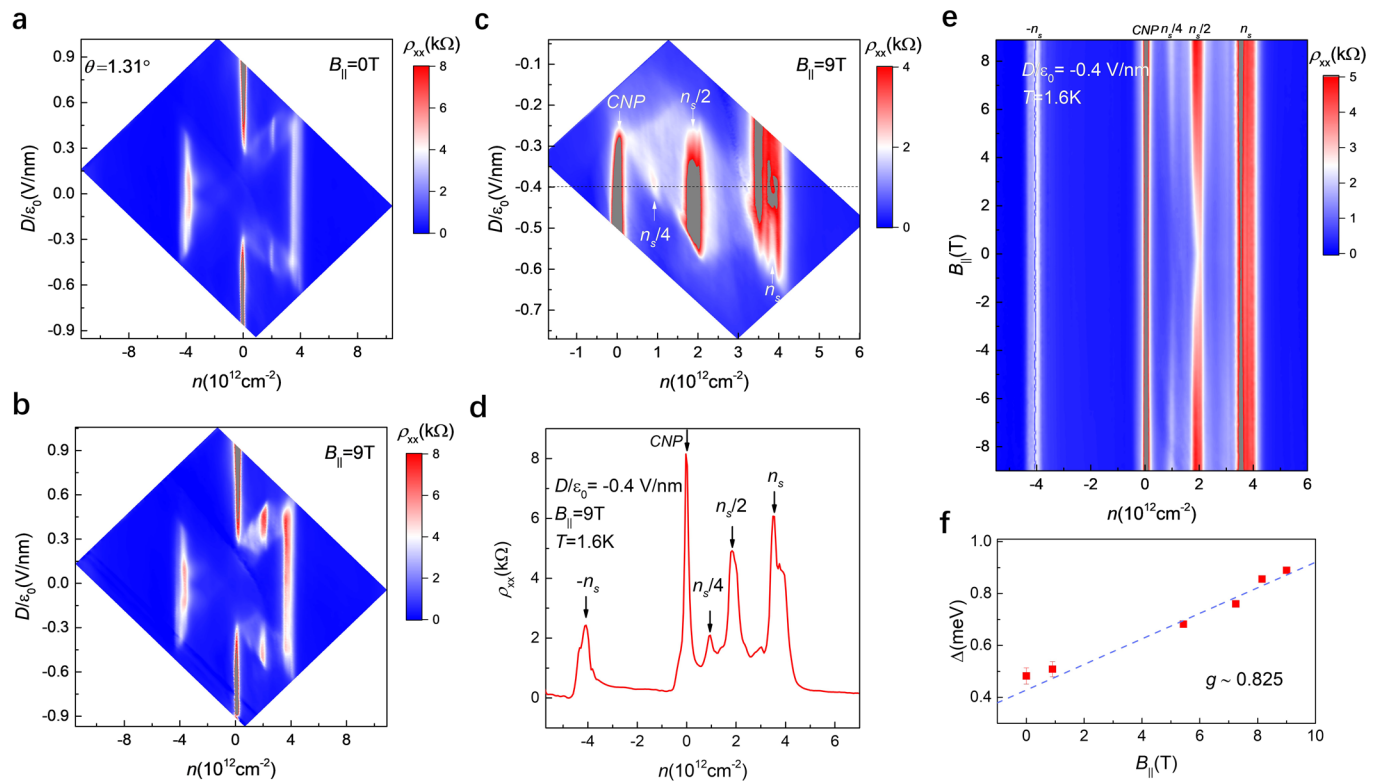
**Extended Data Fig. 6 | Quantum oscillations in the 1.33°-device. a**, Magnetoresistance oscillations in perpendicular magnetic field  $B_{\perp}$  varied from 0T to 9T and at  $D/\epsilon_0 = -0.4 \text{ V/nm}$ . **b**, Schematic of Landau levels observed in **a**. Dark blue lines, light blue lines and red lines track Landau levels fanning from CNP, Landau levels fanning from half filling and fractal Landau levels, respectively.



**Extended Data Fig. 7 | Resistivity as a function of temperature at and near 1/2 and 3/4 fillings in various perpendicular magnetic fields.**

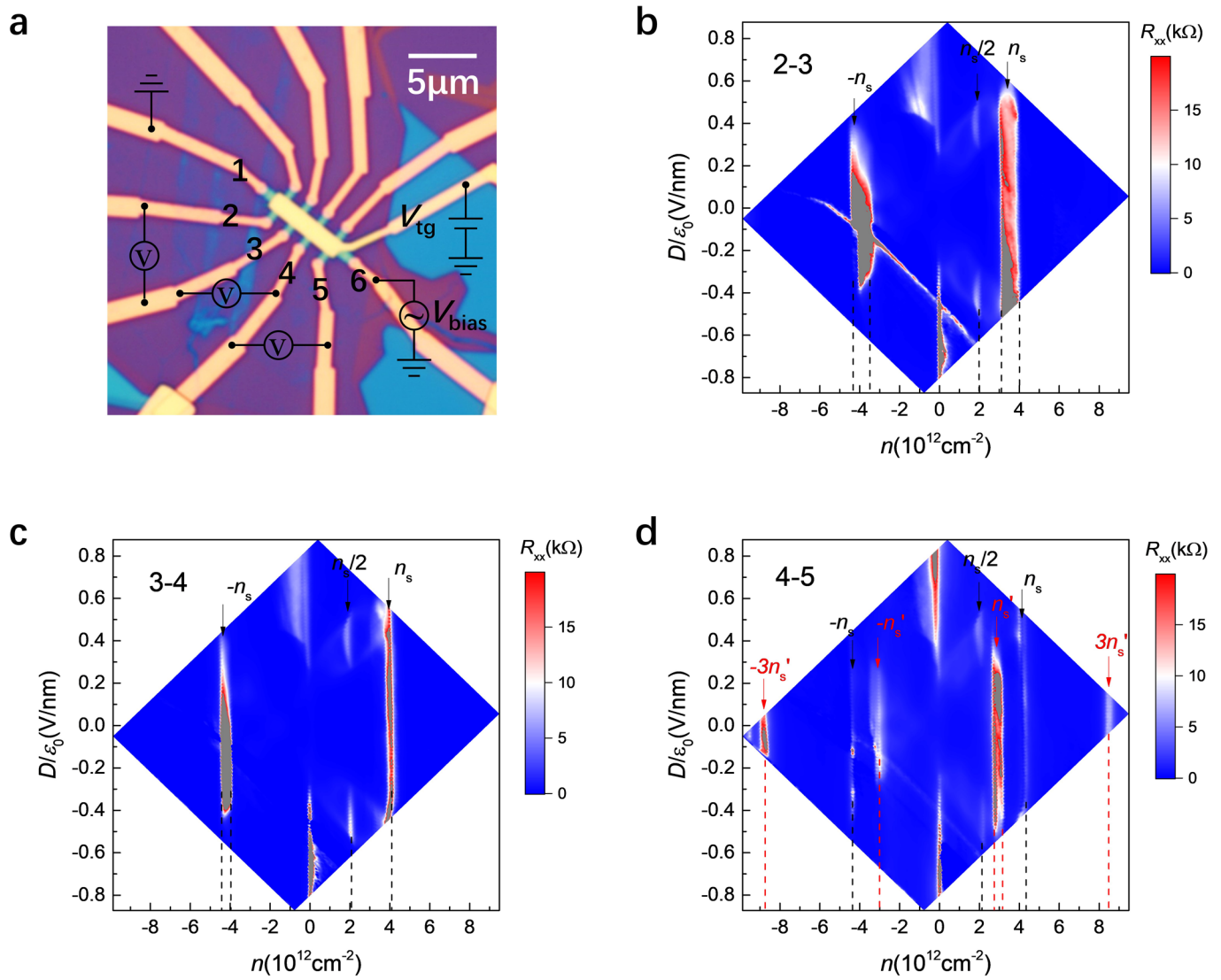
**a, c,** Temperature-dependent resistivity behaviors right at half filling (**a**) and 3/4 filling (**c**). The inset figure in **a** shows thermal activation gaps at  $B_{\perp} = 0\text{T}$ , 1T, 3T and 6T. The fitting is denoted by lines in the main figure according to Arrhenius formula. The 3/4-filling insulating state is induced at  $B_{\perp} = 6\text{T}$ .

**b, d,**  $T$ -dependent resistivity behaviors at electron-doped half filling (**b**) and 3/4 filling (**d**). All the data are acquired in the 1.33°-device.

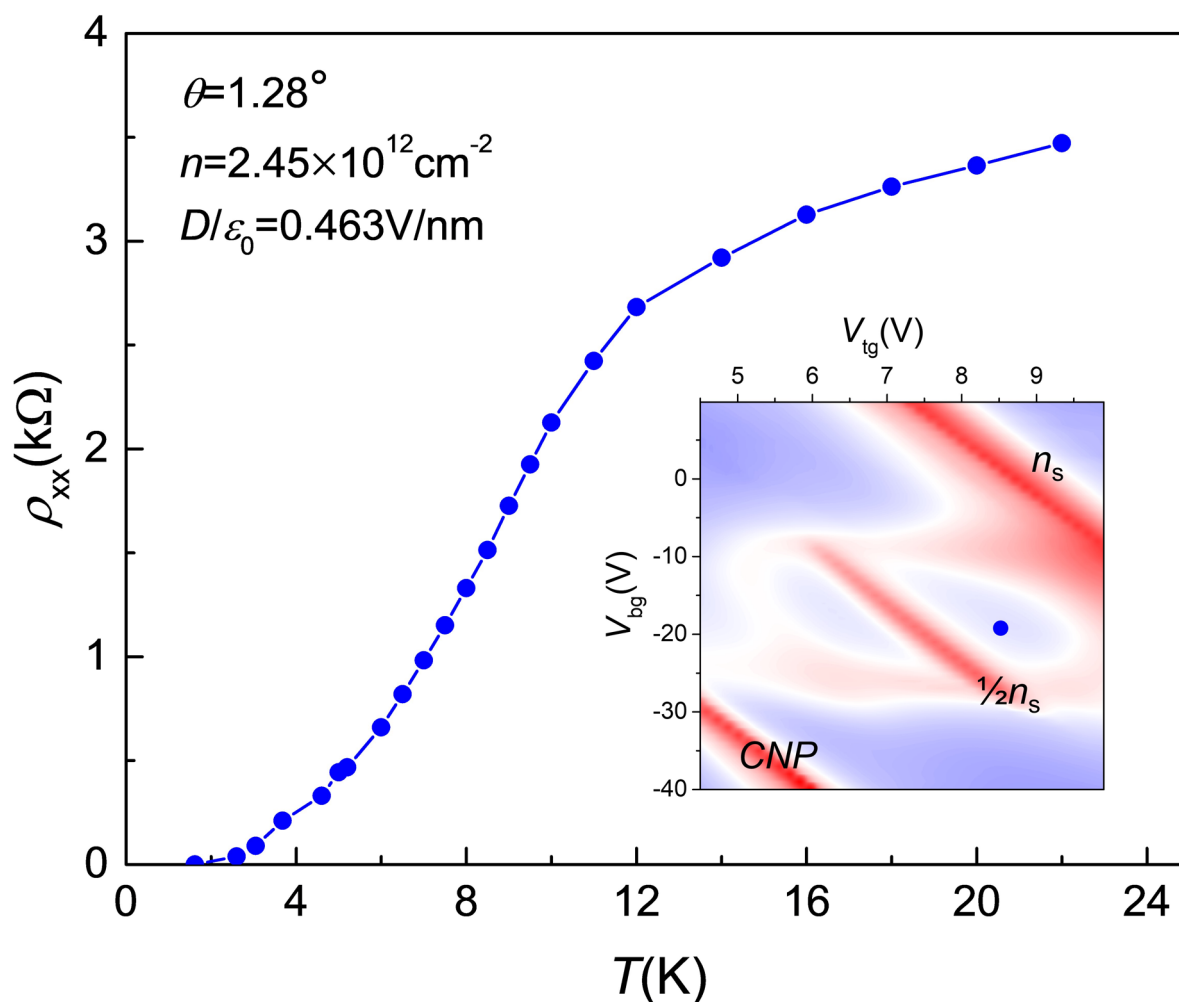


**Extended Data Fig. 8 | Correlated insulators enhanced by parallel magnetic fields in the 1.31°-device.** **a, b**, Resistivity as a function of  $D$  and  $n$  at  $B_{||}=0\text{ T}$  (**a**) and  $B_{||}=9\text{ T}$  (**b**). **c**, Zoomed-in image for clear displaying of  $1/4$  and  $1/2$  filling insulators at  $B_{||}=9\text{ T}$ . **d**, Resistivity versus density  $n$  at  $D/\epsilon_0=-0.4\text{ V/nm}$  corresponding to the dash line in **c**. **e**,  $B_{||}$  dependence of all insulating states, including  $B_{||}$ -induced  $1/4$ -filling and enhanced half-filling correlated states. **f**, A fitted effective  $g$  factor according to the spin-Zeeman effect. The data in **f** show thermal-activation gaps at various  $B_{||}$ . Error bars in **f** are estimated from the uncertainty in the range of simply activated regime.





**Extended Data Fig. 9 | Twist angle inhomogeneity in the 1.33°-device.** **a**, Schematic of measurement configuration and optical image of the 1.33°-device. **b**, **c**, **d**, Resistance color plot versus carrier density  $n$  and displacement field  $D$  at 1.6K acquired between contacts shown in **a**. We could extract twist angle  $\theta=1.33^\circ\pm0.01^\circ$  as well as  $\theta=1.11^\circ\pm0.04^\circ$  between contacts 4 and 5 according to the carrier density  $n_s/2$  or  $n_s$  in **d**. The errors here are estimated from the uncertainty in determining resistance peaks in **d**. The discussed transport data in main text and Methods for 1.33°-device were acquired between contacts 3 and 4.



**Extended Data Fig. 10 | Zero resistivity in the 1.28°-device.** Temperature-varied resistivity data were acquired at  $n = 2.45 \times 10^{12} \text{ cm}^{-2}$  and  $D/\epsilon_0 = 0.463 \text{ V/nm}$ , where a blue dot is located in the inset figure. The inset figure shows resistance mapping as a function of  $V_{bg}$  and  $V_{tg}$  for the 1.28°-device at  $T = 3 \text{ K}$ .